Ion-photoelectron entanglement in photoionization with chirped laser pulses

OPEN ACCESS
IOP Publishing
Journal of Physics B: Atomic, Molecular and Optical Physics
J. Phys. B: At. Mol. Opt. Phys. **55** (2022) 134001 (9pp)
https://doi.org/10.1088/1361-6455/ac6e17

Ion-photoelectron entanglement in photoionization with chirped laser pulses

Marc J J Vrakking*

Max-Born-Institut, Max-Born-Str. 2A, 12489 Berlin, Germany

E-mail: marc.vrakking@mbi-berlin.de

Received 11 March 2022, revised 4 May 2022
Accepted for publication 8 May 2022
Published 9 June 2022

Abstract

The investigation of coherent dynamics induced by photoionization of atoms or molecules by extreme ultra-violet (XUV) attosecond laser pulses requires careful consideration of the degree of ion + photoelectron entanglement that results from the photoionization process. Here, we consider coherent H_2^+ vibrational dynamics induced by photoionization of neutral H_2 by a chirped attosecond laser pulse. We show that chirping the attosecond laser pulse leads to ion + photoelectron entanglement and the transition from a pure to a mixed state. This transition is characterized by evaluating the purity, which is close to unity for a transform-limited attosecond laser pulse and which decreases to a value that is determined by the number of vibrational states populated in the photoionization process for increasing values of the chirp parameter. In the calculations, the vibrational dynamics is probed by calculating time-delayed dissociation of the H_2^+ cation by a short ultra-violet (UV) laser pulse. Independent of the magnitude of the chirp, the coherent vibrational dynamics can be recovered by recording the XUV-UV delay-dependent kinetic energy release in coincidence with the kinetic energy of the accompanying photoelectron.

Keywords: attosecond science, photoionization, entanglement, coherence

(Some figures may appear in colour only in the online journal)

1. Introduction

Although well-established as the theory that is required to correctly describe observable phenomena in atoms and molecules, several aspects of quantum mechanics remain baffling, since they force the acceptance of a view of reality that seems to conflict with the behaviour that is commonly observed on macroscopic time- and length scales. This is particularly true for quantum entanglement, which dictates the persistence of measurable correlations between distinguishable quantum systems that have a common origin but that no longer interact with each other.

Quantum entanglement has its origin in the famous EPR paradox [1], which to Einstein suggested the necessity of the inclusion of hidden variables within quantum mechanics. This view was later refuted by Bell, who proposed an experiment to rule out the possible existence of hidden variables [2] and showed that correlations between measurements on entangled particles can be stronger than the correlations that are possible in classical systems. Violations of Bell's inequality were subsequently demonstrated in several pioneering experiments (see e.g. [3, 4]), confirming the correctness of the quantum mechanical description of entangled systems, and confirming the nonlocality that they encompass. In the years since Bell's paper and the experimental demonstrations of entanglement, it has been appreciated that entanglement can be exploited in quantum information processing [5], and in remarkable feats such as quantum key distribution [6], quantum computing [7] and quantum teleportation [8]. Moreover, decoherence theory has explained how entanglement of quantum systems with an

* Author to whom any correspondence should be addressed.

environment leads to the emergence of the classical results that are observed in experiments [9–11].

Recently, the possible role that quantum entanglement can play in attosecond science, or—more generally—experiments involving photoionization [12], has started drawing increasing attention [13–17]. Attosecond pulses formed by high-harmonic generation necessarily have photon energies in the extreme-ultraviolet (XUV) or soft x-ray spectral region [18], and hence are ionizing radiation for any sample. Photoionization leads to the formation of an ion + photoelectron pair, and leads to entanglement whenever the ion + photoelectron wavefunction cannot simply be written as the direct product of an ionic wavefunction and a photoelectron wavefunction, i.e.

$$\Psi \neq \psi_{\text{ion}} \otimes \psi_{\text{photoelectron}} \tag{1}$$

but instead can only be written as a superposition of such products, i.e.

$$\Psi \sim \sum_{\alpha,\beta} \psi_{\text{ion},\alpha} \otimes \psi_{\text{photoelectron},\beta}, \tag{2}$$

where α and β are the full set of quantum numbers needed to characterize the properties of both the ion and the photoelectron. We may expect quantum entanglement to be very common in attosecond science, since situations abound where photoionization leads to different combinations of cationic internal (electronic, vibrational, rotational) states and their accompanying photoelectron momentum states. Accordingly, several contributions have appeared in the literature pointing to the possible role of quantum entanglement in attosecond pump-probe experiments [13–16], and we have recently, following a prediction in [17], reported experiments where the degree of vibrational coherence in H_2^+ ions formed by photoionization by a sequence of two attosecond XUV pulses (or two attosecond pulse trains) could be controlled by the delay between these two pulses [19].

In this paper, the calculations reported in [17] are extended, and calculations are described where a neutral, aligned H_2 molecule is exposed to a chirped attosecond XUV pulse that induces photoionization, followed by a short UV pulse that dissociates the cation. Consistent with the intuitive notion that pump-probe experiments can time-resolve phenomena that occur on a timescale that is comparable or longer than the cross-correlation between the pump- and probe-lasers, H^+ kinetic energy release (KER) distributions are calculated as a function of XUV-UV pump-probe delay that reveal the coherent H_2^+ vibrational dynamics for moderate values of the chirp, and that show a disappearance of the delay-dependent signatures of this vibrational dynamics for larger chirp. This is accompanied by a significant reduction of the evaluated purity of the ion-photoelectron wavefunction. However, the cationic vibrational dynamics can be recovered for arbitrary values of the chirp, when the KER distributions are calculated *in coincidence* with the photoelectron momentum. This is a manifestation of the fact that, whereas the ionic vibrational coherence is lost for large values of the chirp, the coherence in the entangled ion + photoelectron system is fully maintained.

The organization of the paper is as follows. Section 2 describes the computational method, which amounts to solving a 2D time-dependent Schrödinger equation (TDSE) for an aligned H_2 molecule, with one computational degree of freedom reserved for motion of the photoelectron along the laser polarization axis, and one for the internuclear motion. The time-dependent surface flux (TSURFF) method [20] is used to calculate the probability that a certain H^+ KER occurs in coincidence with the formation of a photoelectron with a certain kinetic energy [21]. Section 3 presents the main computational results, as well as their interpretation in terms of a simple interference model, where the phase difference between two quantum pathways is considered that lead to the same final photoelectron momentum, but that differ in the H_2^+ vibrational state that is formed in the attosecond ionization process. This model quantitatively explains the observed linear dependence of the delays where constructive two-path interference occurs on the photoelectron momentum. Section 3 moreover contains a determination of the purity of the ion + photoelectron wave function that is obtained by solving the TDSE, as well as a comparison of this purity to a simple model that takes into account the influence of the chirp on the spectral amplitude of the XUV attosecond pulse.

2. Methodology

The computational method used in this paper largely follows the method that was described by Yue and Madsen in reference [21]. This method was extended by deriving the relevant equations for dissociative ionization in a two state-model including the $1s\sigma_g$ and $2p\sigma_u$ electronic states of H_2^+, effectively combining the approaches used in sections B and C of [21]. Since additionally a somewhat different numerical implementation was chosen, a summary of the computational method is given below.

The starting point of the numerical approach is the expression for the wave function describing an H_2^+ molecular ion (in the $1s\sigma_g$ or $2p\sigma_u$ electronic state, treated in the Born–Oppenheimer approximation) in combination with a photoelectron resulting from the ionization of neutral H_2 by the attosecond pulse:

$$\Psi(R,x,t) = \Psi_g(R,x,t)\,\phi_g(R,y) + \Psi_u(R,x,t)\,\phi_u(R,y), \tag{3}$$

where R, x and y are the internuclear distance and the coordinates of the free and the bound electron, respectively. Insertion of this wave function into the TDSE yields the following equations for the ion + photoelectron wave packets associated with the $1s\sigma_g$ and $2p\sigma_u$ H_2^+ electronic states:

$$\begin{aligned} i\dot{\Psi}_g(R,x,t) = &\left\{T_N + T_e + V_{1s\sigma_g}(R) + V_C(R,x)\right. \\ &\left. + V_{\text{laser}}(x)\right\}\Psi_g(R,x,t) + \langle\phi_g(R,y)| \\ &V_{\text{laser}}(y)\,|\phi_u(R,y)\rangle\,\Psi_u(R,x,t) \\ i\dot{\Psi}_u(R,x,t) = &\left\{T_N + T_e + V_{2p\sigma_u}(R) + V_C(R,x)\right. \\ &\left. + V_{\text{laser}}(x)\right\}\Psi_u(R,x,t) + \langle\phi_u(R,y)| \\ &V_{\text{laser}}(y)\,|\phi_g(R,y)\rangle\,\Psi_g(R,x,t) \end{aligned}, \tag{4}$$

where $T_N = \frac{-1}{2\mu_R}\left(\frac{\delta^2}{\delta R^2}\right)$ and $T_e = \frac{-1}{2\mu_e}\left(\frac{\delta^2}{\delta x^2}\right)$, μ_R and μ_e are the reduced masses of the H_2^+ cation and the photoelectron, respectively, $V_{1s\sigma_g}(R)$ and $V_{2p\sigma_u}(R)$ are the potential energy curves of the $1s\sigma_g$ and $2p\sigma_u$ H_2^+ cationic states [22], and $V_C(R,x)$ describes the Coulomb interaction of the photoelectron with the H_2^+ cation, given by a softcore Coulomb potential

$$V_C(R,x) = \frac{-1}{2\sqrt{\left(x+\frac{R}{2}\right)^2+a}} - \frac{1}{2\sqrt{\left(x-\frac{R}{2}\right)^2+a}} \tag{5}$$

and $V_{laser}(x)$ and $V_{laser}(y)$ describe the interaction of the photoelectron and the bound electron with the laser field(s) F_{laser}. In what follows, the approximation

$$\begin{aligned}&\langle\phi_g(R,y)|\, V_{laser}(y)\,|\phi_u(R,y)\rangle \\ &\quad = \langle\phi_u(R,y)|\, V_{laser}(y)\,|\phi_g(R,y)\rangle \\ &\quad \approx F_{laser}\frac{R}{2}\end{aligned} \tag{6}$$

is used [23]. This eliminates the bound electron from the problem, and reduces the TDSE to a 2D equation for $\Psi_g(R,x,t)$ and $\Psi_u(R,x,t)$. In the softcore Coulomb potential (equation (3)) a value of $a = 1.5$ was used, leading to an H_2 ground state energy of -0.612 a.u., compared to the experimental value of -0.568 a.u. [24].

The physical situation that we seek to describe is photoionization of neutral H_2 by a chirped attosecond XUV pulse, followed by dissociation of the H_2^+ cation by a UV probe pulse. The latter interaction potentially takes place at long time delays with respect to the XUV ionization, when the photoelectron is far removed from the H_2^+ cation. This situation is conveniently handled by application of the TSURFF formalism, where one exploits the fact that after dissociative ionization, for $|x| > x_S$ and $R > R_S$, $V_C(R,x)$ and $V_{1s\sigma_g/2p\sigma_u}(R)$ become negligible and $\Psi_{g/u}(R,x,t)$ can be expanded in a product of Coulomb–Volkov wave functions and plane waves according to

$$\Psi_g(R,x,t) = \int dp \int dk\; b_{pk,g}(t)\,\phi_p(x,t)\,\chi_k(R,t) \tag{7a}$$

$$\Psi_u(R,x,t) = \int dp \int dk\; b_{pk,u}(t)\,\phi_p(x,t)\,\chi_k(R,t)\,, \tag{7b}$$

where

$$\phi_p(x,t) = \frac{1}{\sqrt{2\pi}}\,\exp\left[i\left(px - \frac{p^2 t}{2\mu_e} - \frac{p}{\mu_e}\int^t A(t')\,dt'\right)\right] \tag{8}$$

and

$$\chi_k(R,t) = \frac{1}{\sqrt{2\pi}}\,\exp\left[i\left(kx - \frac{k^2 t}{2\mu_R}\right)\right] \tag{9}$$

with p and k the photoelectron and nuclear momentum, respectively.

According to equation (7) the expansion coefficients $b_{pk,g}(t)$ and $b_{pk,u}(t)$ are given as

$$\begin{aligned}b_{pk,g}(t) &= \langle\phi_p(x,t)\,|\langle\chi_k(R,t)\,|\theta_e\theta_N|\Psi_g(R,x,t)\rangle \\ b_{pk,u}(t) &= \langle\phi_p(x,t)\,|\langle\chi_k(R,t)\,|\theta_e\theta_N|\Psi_u(R,x,t)\rangle\end{aligned}\,, \tag{10}$$

where $\theta_e = 1$ for $|x| \geqslant x_S$, and $\theta_e = 0$ for $|x| < x_S$, and where $\theta_N = 1$ for $R \geqslant R_S$, and $\theta_N = 0$ for $R < R_S$. The coefficients $b_{pk,g}(t)$ and $b_{pk,u}(t)$ define the so-called joint energy spectrum (JES), which represents the probability that a photoelectron with a kinetic energy $E_e = \frac{p^2}{2\mu_e}$ is measured in combination with a KER of $\frac{k^2}{2\mu_R}$. Following the methodology of reference [21], the following expressions for the time evolution of $b_{pk,g}(t)$ and $b_{pk,u}(t)$ can be obtained:

$$\begin{aligned}b_{pk,g}(T) &= \int_{-\infty}^{T} dt \frac{d}{dt}\,\langle\phi_p(x,t)\,|\langle\chi_k(R,t)\,|\theta_e\theta_N|\Psi_g(R,x,t)\rangle \\ &\approx i\int_{-\infty}^{T} dt\,\big[\langle\chi_k(R,t)\,|[T_N,\theta_N]|\langle\phi_p(x,t)\,|\theta_e \\ &\quad |\Psi_g(R,x,t)\rangle - \langle\phi_g|V_{laser}(y)|\phi_u\rangle\, b_{pk,u}(t)\big] \\ &\doteq i\int_{-\infty}^{T} dt\,\big[\langle\chi_k(R,t)\,|[T_N,\theta_N]|\, h_g(R,t) \\ &\quad - \langle\phi_g|V_{laser}(y)|\phi_u\rangle\, b_{pk,u}(t)\big] \\ b_{pk,u}(t) &= \int_{-\infty}^{T} dt \frac{d}{dt}\,\langle\phi_p(x,t)\,|\,\langle\chi_k(R,t)|\theta_e\theta_N|\Psi_u(R,x,t)\rangle \\ &\approx i\int_{-\infty}^{T} dt\,\big[\langle\chi_k(R,t)\,|[T_N,\theta_N]|\,\langle\phi_p(x,t)|\theta_e|\Psi_u(R,x,t)\rangle \\ &\quad - \langle\phi_u|V_{laser}(y)|\phi_g\rangle\, b_{pk,u}(t)\big] \\ &\doteq i\int_{-\infty}^{T} dt\,\big[\langle\chi_k(R,t)|[T_N,\theta_N]|\, h_u(R,t) \\ &\quad - \langle\phi_u|V_{laser}(y)|\phi_g\rangle\, b_{pk,u}(t)\big]\,.\end{aligned} \tag{11}$$

Note that at this point our numerical approach differs from the one followed in [21], where $h_g(R,t) = \langle\phi_p(x,t)|\,\theta_e\,|\Psi_g(R,x,t)\rangle$ was expanded in a sine basis. The functions $h_g(R,t)$ and $h_u(R,t)$ encode the photoelectron flux that moves beyond $|x| > x_S$, and act as a source term for the integration of $b_{pk,g}(T)$ and $b_{pk,u}(T)$. They can be obtained by integration, considering that

$$\begin{aligned}\dot{h}_g(R,t) &= \left\langle\dot{\phi}_p(x,t)\,|\theta_e|\Psi_g(R,x,t)\right\rangle + \left\langle\phi_p(x,t)\,|\theta_e|\dot{\Psi}_g(R,x,t)\right\rangle \\ &= i\,\langle\phi_p(x,t)\,|\,[(T_e + V_{laser}(x)),\theta_e]\,|\Psi_g(R,x,t)\rangle \\ &\quad - i\left(T_N + V_{1s\sigma_g}(R)\right) h_g(R,t) \\ &\quad - i\,\langle\phi_g|V_{laser}(y)|\phi_u\rangle\, h_u(R,t) \\ \dot{h}_u(R,t) &= \left\langle\dot{\phi}_p(x,t)\,|\theta_e|\Psi_u(R,x,t)\right\rangle + \left\langle\phi_p(x,t)\,|\theta_e|\dot{\Psi}_u(R,x,t)\right\rangle \\ &= i\,\langle\phi_p(x,t)\,|\,[(T_e + V_{laser}(x)),\theta_e]\,|\Psi_u(R,x,t)\rangle \\ &\quad - i\left(T_N + V_{2p\sigma_u}(R)\right) h_u(R,t) \\ &\quad - i\,\langle\phi_u|V_{laser}(y)|\phi_g\rangle\, h_g(R,t).\end{aligned} \tag{12}$$

Making use of the properties of the Heavyside function, the first part of the expression for $\dot{h}_g(R,t)$ can be evaluated according to [21]

$$\begin{aligned} & i\left\langle\phi_p(x,t)\right|\left[\left(T_e+V_{\text{laser}}(x)\right),\theta_e\right]\left|\Psi_g(R,x,t)\right\rangle \\ &= i\int dx\phi_p^*(x,t)\left[-\frac{1}{2\mu_e}\delta'(x-x_s)-\text{sgn}(x)\,\delta\left(|x|-x_s\right)\right. \\ &\qquad \left.\times\left(\frac{1}{\mu_e}\frac{\delta}{\delta x}+i\beta A(t)\right)\right]\Psi_g(R,x,t) \\ &= \phi_p^*(x_s,t)\left\{\frac{p}{2\mu_e}+\beta A(t)-\frac{i}{2\mu_e}\frac{\delta}{\delta x}\right\}\Psi_g(R,x_s,t) \\ &\quad -\phi_p^*(-x_s,t)\left\{\frac{p}{2\mu_e}+\beta A(t)-\frac{i}{2\mu_e}\frac{\delta}{\delta x}\right\}\Psi_g(R,-x_s,t), \end{aligned} \tag{13}$$

where $\beta=(m_H+1)/m_H$, with m_H the proton mass and with an equivalent equation for the expression for $\dot{h}_u(R,t)$. In practice, $h_g(R,t)$ and $h_u(R,t)$ are integrated by means of a Crank–Nicolson integration scheme. Once $h_g(R,t)$ and $h_u(R,t)$ are available, they are used within equation (11) to evaluate (once more by numerical integration) the coefficients $b_{pk,g}(t)$ and $b_{pk,u}(t)$. In doing so, the first term appearing in the integral in equation (9) is evaluated, again making use of the properties of the Heavyside function, as

$$\begin{aligned} & \left\langle\chi_k(R,t)\right|\left[T_{\text{N}},\theta_{\text{N}}\right]\left|h_g(R,t)\right. \\ &= \int dR\,\chi_k^*(R,t)\left[\frac{-1}{2\mu_R}\delta'(R-R_s)+2\delta\left(|R|-R_s\right)\frac{\delta}{\delta R}\right] \\ &\quad \times h_g(R_s,t). \end{aligned} \tag{14}$$

With an equivalent expression for the matrix element containing $h_u(R,t)$.

3. Computational results

In the 2D TDSE calculations that were performed to calculate the photoelectron flux at $x=x_s$, the ion + photoelectron wavefunction was propagated on a 2D grid with $R\leqslant 12.8$ a.u.($\delta R=0.025$ a.u.) and $|x|\leqslant 409.6$ a.u.($\delta x=0.4$ a.u.), with absorbing boundaries placed at $R=10$ a.u. and $|x|=250$ a.u., respectively. The photoelectron flux was evaluated at $|x_s|=200$ a.u. and in the subsequent TSURFF calculations, the radial flux was evaluated at $R_s=9.5$ a.u. In the calculations of the purity, the electron grid was extended to $|x|=6553.6$ a.u. and the electron absorbing boundary was placed at $|x|=6000$ a.u.

The chirped XUV pulse was parametrized as a Gaussian pulse

$$\begin{aligned} E_{\text{XUV}}(t) = E_0\,\exp\left[-(1+i\alpha)\left(\frac{t-t_0}{\tau_G}\right)^2\right] \\ \times\exp\left[i\omega_{\text{XUV}}(t-t_0)\right]/\left(1+\alpha^2\right)^{1/4} \end{aligned} \tag{15}$$

with α as the chirp parameter, and

$$\tau_G=\tau_{G,0}\left(1+\alpha^2\right)^{1/2}, \tag{16}$$

where

$$\tau_{G,0}=1.9364\frac{N_{\text{cycles}}}{\omega_{\text{XUV}}}. \tag{17}$$

With this definition of τ_G, the full-width-at-half-maximum pulse duration of the laser pulse is the same as that of an N_{cycles} long cos-squared laser pulse when $\alpha=0$, and the pulse duration increases by a factor α when $\alpha\gg 1$. The pulse bandwidth is independent of α. Calculations were performed with $\omega_{\text{XUV}}=0.8$ a.u. (21.8 eV) and $N_{\text{cycles}}=10$, leading to $\tau_{G,0}=24.2$ a.u. (585 attoseconds). The calculations were performed with $E_0=0.001$ a.u., corresponding to a peak intensity of 3.51×10^{10} W cm^{-2} when $\alpha=0$. The chirp parameter α was varied between -100 and 100. The UV pulse was parametrized as a 10-cycle long, chirp-free, cos-squared pulse with a peak field strength $E_{\text{UV}}=0.004$ a.u. (corresponding to a peak intensity of 5.62×10^{11} W cm^{-2}), and with a carrier frequency of 0.1 a.u. (correspondingto a wavelength of 455 nm). The joint photoelectron-ion momentum distribution was calculated for photoelectron momenta $p\in\langle 0.5,0.9\rangle$ a.u. and nuclear momenta $k\in\langle 0,30\rangle$ a.u. A representative set of results is shown in figures 1(a)–(g), where the joint photoelectron-ion momentum distribution is shown for a delay of 12 600 a.u. (305 fs) between the XUV and UV pulses, for 7 values of the chirp parameter α between -100 and 100. Note that for $|\alpha|=100$, the value of τ_G is 58.5 fs, i.e. well beyond the vibrational period of the H_2^+ cation.

Calculations like the ones shown in figures 1(a)–(g) were performed for 750 XUV-UV delays between 0 and 29 960 a.u. (724 femtoseconds). Figures 1(h)–(n) show the joint photoelectron-ion momentum distribution evaluated at $k=9.9$ a.u. (i.e. in the middle of the unstructured nuclear momentum distribution, see figures 1(a)–(g). Figure 1(k) shows the result for $\alpha=0$. As expected, and in agreement with previous experiments [19, 25], the delay dependence shows oscillatory signals that reflect a significant increase in the H_2^+ dissociation probability by the UV pulse whenever the vibrational wave packet that is excited by the photoionization is located near the outer turning point of the $1s\sigma_g$ potential energy curve. Figure 1(k) moreover reveals the periodic dephasing and rephasing that is expected and observed for such a vibrational wave packet. A striking feature of the joint photoelectron-ion momentum distributions that are shown in figures 1(a)–(c) and (e)–(g) for finite values of the chirp is the appearance of a fringe structure along the photoelectron momentum direction. As revealed by figures 1(h)–(j) and (l)–(o), these fringes are a consequence of the existence of a slanted structure in the probability for dissociation as a function of the photoelectron momentum and the XUV-UV delay.

The appearance of these slanted structures can be explained by considering the interference between two pathways that lead to the same final photoelectron and nuclear momentum, but for which the absorbed XUV photon energy differs in such a manner that different ionic vibrational states are formed in the ionization process by the XUV pump laser. Based on equation (13) the carrier frequency of the chirped XUV pulse

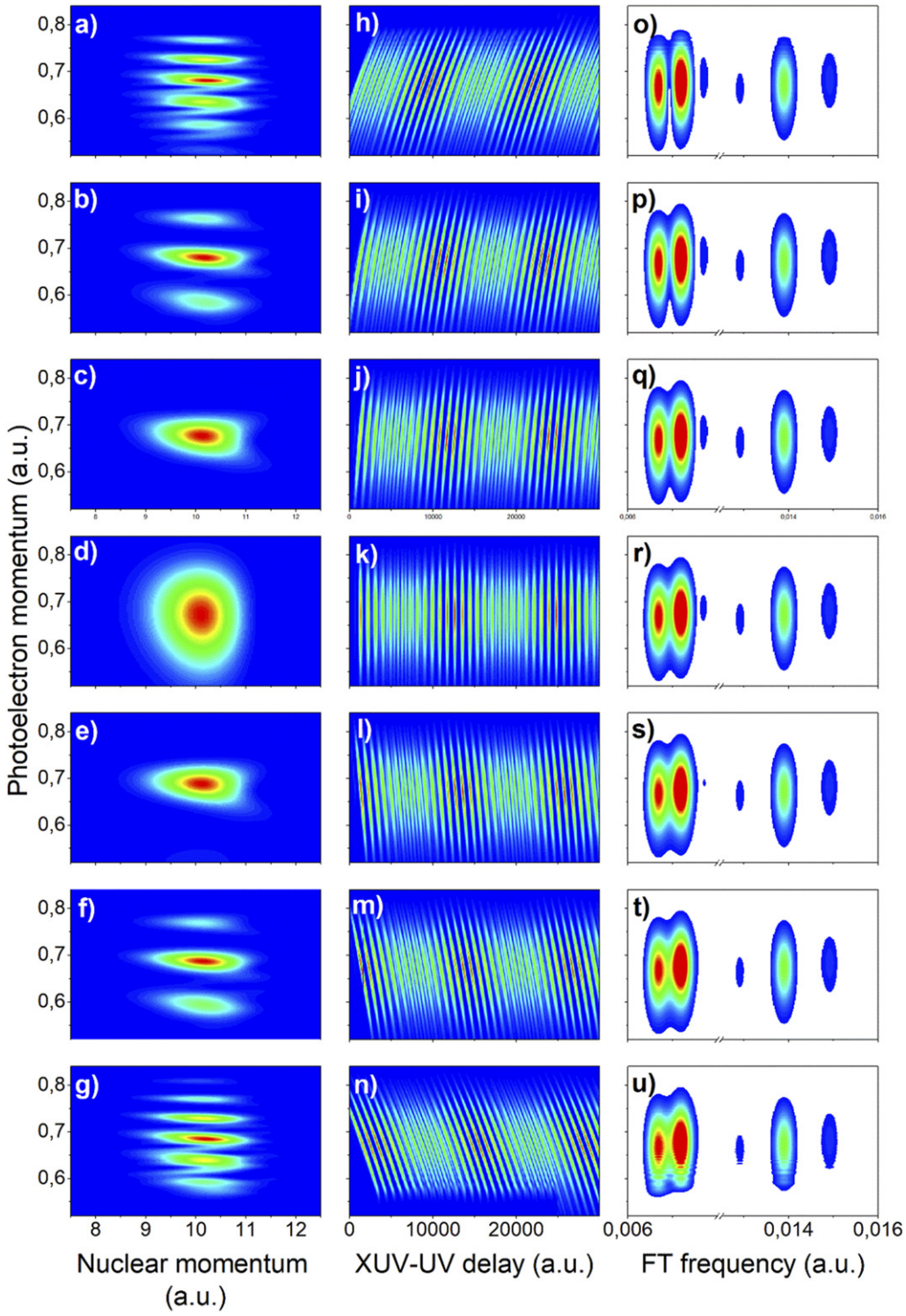

Figure 1. (a)–(g) Joint photoelectron-ion momentum distribution, calculated for the ionization of H_2 by a chirped XUV laser pulse, with the chirp parameter given by (a) $\alpha = -100$, (b) $\alpha = -50$, (c) $\alpha = -25$, (d) $\alpha = 0$, (e) $\alpha = 25$, (f) $\alpha = 50$ and (g) $\alpha = 100$, followed by dissociation by a UV laser pulse that is delayed by 12 600 a.u. (305 fs). See the main text for the definition of the pulses and all other laser parameters; (h)–(n) joint photoelectron-ion momentum distribution evaluated at $k = 9.9$ a.u., as a function of the delay between the XUV and UV pulses; (o)–(u) Fourier transform power spectrum of the data shown in figures 1(h)–(n), revealing the two-level quantum beats responsible for the observed time dependencies.

is given by

$$\omega(t) = \frac{d\varphi(t)}{dt} = \omega_{\mathrm{XUV}} - 2\alpha(t - t_0)/\tau_G^2. \tag{18}$$

Considering an ionic state with energy E_1 that is formed in combination with a photoelectron with momentum p, a resonance condition occurs for

$$t_1 = t_0 + \frac{\tau_G^2}{2\alpha}\left[\omega_{\mathrm{XUV}} - E_1 - \frac{1}{2}p^2.\right] \tag{19}$$

A similar equation may be written for the time t_2 when a resonance condition occurs for an ionic state with energy E_2. Once photoionization has occurred at time $t_{1,2}$, the ion + photoelectron system evolves at an energy of $E_{1,2} + \frac{1}{2}p^2$ until the UV probe laser projects both ionic states onto a common final state (corresponding to the dissociation into an $H + H^+$ with nuclear momentum k, accompanied by a photoelectron with momentum p). The phases associated with both quantum paths are given by the sum of the phase of the XUV field at $t = t_{1,2}$ and the evolution at energy $E_{1,2} + \frac{1}{2}p^2$ between $t = t_{1,2}$ and $t = t_{\mathrm{f}}$, that is

$$\begin{aligned}\varphi_{1,2} = \omega_{\mathrm{XUV}}\left(t_{1,2} - t_0\right) - \alpha\frac{\left(t_{1,2} - t_0\right)^2}{\tau_G^2} \\ + \left(E_{1,2} + \frac{1}{2}p^2\right)\left(t_{\mathrm{f}} - t_{1,2}\right)\end{aligned}. \tag{20}$$

From this, it follows that constructive interference between the two quantum paths occurs when

$$\begin{aligned}\varphi_2 - \varphi_1 = \left(E_2 - E_1\right)t_{\mathrm{f}} + \frac{\tau_G^2}{4\alpha}\left(E_2 - E_1\right) \\ \times\left(E_1 + E_2 + p^2 - 2\omega_{\mathrm{XUV}}\right) = 2n\pi\end{aligned} \tag{21}$$

implying that

$$t_{\mathrm{f}} = \frac{2n\pi}{\left(E_2 - E_1\right)} - \frac{\tau_G^2}{4\alpha}\left(E_1 + E_2 + p^2 - 2\omega_{\mathrm{XUV}}\right). \tag{22}$$

From this it follows that there exists a correlation between the photoelectron momentum p and the time for which a constructive interference occurs in the detected signal, according to

$$\frac{\partial t_{\mathrm{f}}}{\partial p} = -\frac{\tau_G^2}{2\alpha}p. \tag{23}$$

This is the slope that can be recognized in figures 1(h)–(j) and (l)–(o). The existence of this slope leads to the fact that in the absence of a determination of the photoelectron momentum p the observed wave packet motion disappears for a large enough chirp. This is illustrated in figures 2(a)–(g), where the nuclear momentum distribution is plotted as a function of XUV-UV delay for 7 values of the chirp parameter α between -100 and 100. Note that this nuclear momentum distribution was obtained by integrating the joint photoelectron-ion momentum distributions at each XUV-UV delay over the photoelectron momentum. Integration of these distributions over nuclear momentum leads to the total fragment ion yields as a function of XUV-UV delay that are shown in figures 2(h)–(n). While the wave packet motion leads to oscillatory structures in calculations for $\alpha = 0$ or $|\alpha| = 25$, the wave packet motion is no longer visible in calculations with $|\alpha| = 50$ or $|\alpha| = 100$, consistent with the fact that under these conditions the cross-correlation between the pump- and the probe pulses exceeds the vibrational period.

Interestingly, the vibrational coherence can be recovered when the photoelectron is measured in coincidence. This is shown in figures 1(o)–(u), where Fourier transform power spectra are shown for the joint photoelectron-ion momentum distribution as a function of the delay between the XUV and UV pulses evaluated at $k = 9.9$ a.u. (shown in figures 1(h)–(n)). If the photoelectron momentum is measured in coincidence with the H^+ momentum distribution, then the vibrational wave packet motion can be observed regardless of the value of the chirp.

The disappearance of the wave packet motion in figure 3 for increasing values of the chirp can be related to the way in which the system evolves from a pure state to a mixed state. This trend can be quantified by evaluating the purity of the ion + photoelectron wavefunction. The purity can be obtained from the reduced ionic density matrix, which itself is obtained from the density matrix by tracing over the photoelectron degrees of freedom.

For a wavefunction that depends on two degrees of freedom R and x, the density matrix is given as

$$\rho_{Rx,R'x'}(t) = \Psi_{\mathrm{ion}}(R, x, t)\Psi_{\mathrm{ion}}{}^*(R', x', t). \tag{24}$$

In this expression, a subscript 'ion' has been added to the wave function, in order to emphasize that we are only interested in the part of the wave function that corresponds to ionization of the H_2 molecule by the XUV pulse. Normalization of the wave function of the ionized system implies that

$$\iint dR\,dx|\Psi_{\mathrm{ion}}(R, x, t)|^2 = 1. \tag{25}$$

Alternatively, the density matrix can be written using an expansion of the $H_2{}^+$ wave function into a coherent superposition of $H_2{}^+$ vibrational states, i.e.

$$\rho_{vx,v'x'}(t) = \Psi_{\mathrm{ion}}(v, x, t)\Psi_{\mathrm{ion}}{}^*(v', x', t) \tag{26}$$

and this is the form we will use from hereon.

Normalization of this wavefunction implies that

$$\sum_v \int dx|\Psi_{\mathrm{ion}}(v, x, t)|^2 = 1. \tag{27}$$

Using the $H_2{}^+$ vibrational state basis, the reduced ionic density matrix is evaluated as

$$\rho_{v,v'}(t) = \int dx\Psi(v, x, t)\Psi^*(v', x', t). \tag{28}$$

The purity is the trace over the square of the reduced ionic density matrix, i.e.

$$\mathrm{Purity} = \mathrm{Tr}\left(\rho^2\right) = \sum_v \rho_{v,v'}{}^2(t). \tag{29}$$

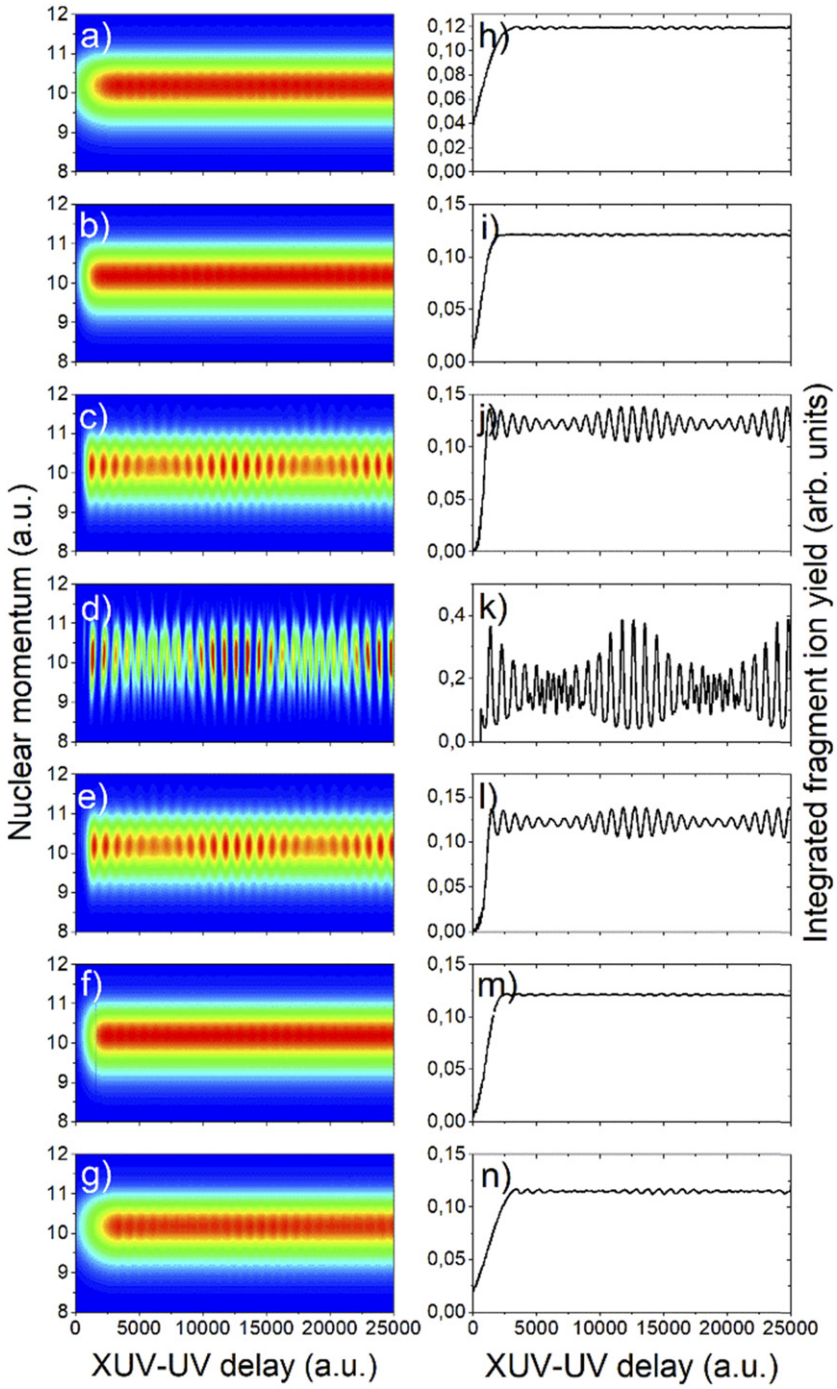

Figure 2. (a)–(g) Nuclear momentum distributions obtained by integrating the joint photoelectron-ion momentum distribution over the photoelectron momentum, calculated for the ionization of H_2 by a chirped XUV laser pulse, with the chirp parameter given by (a) $\alpha = -100$, (b) $\alpha = -50$, (c) $\alpha = -25$, (d) $\alpha = 0$, (e) $\alpha = 25$, (f) $\alpha = 50$ and (g) $\alpha = 100$, followed by dissociation by a UV laser pulse at a variable time delay. See the main text for the definition of the pulses and all other laser parameters; (h)–(n) delay-dependent fragment ion yield, obtained by integrating the distributions shown in (a)–(g) over the nuclear momentum.

From this expression for the purity, one can recognize that the purity is large (i.e. approaching a value of 1) when the off-diagonal matrix elements of the reduced ionic density matrix are at their maximal values. This occurs when the photoelectron wave functions accompanying the formation of vibrational states v and v' are identical or very similar (see equation (28)). By contrast, the purity is minimal when the off-diagonal reduced ionic density matrix elements are zero (i.e. $\rho_{v,v'}(t) = 0$). This situation occurs when the photoelectron wave functions accompanying vibrational level v and v' are orthogonal, in other words, when the ion + photoelectron system is entangled. According to figure 3, which shows the purity of the ion + photoelectron wavefunction calculated according to equation (29) as a function of the chirp parameter α (black curve), the purity approaches a minimal asymptotic value and the degree of entanglement becomes maximal for

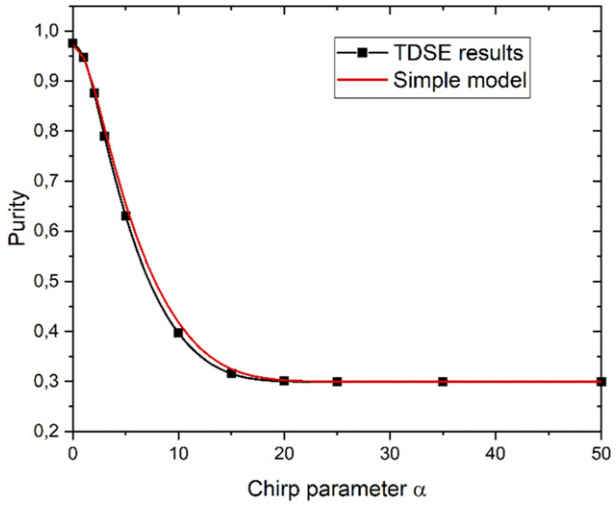

Figure 3. Evolution of the purity of the ion + photoelectron wave function as a function of the chirp of the XUV pulse used in the calculations. The purity was determined in two ways. On the one hand, the purity was extracted from the total ion + photoelectron wave function that was calculated in TDSE calculations using the laser pulse shapes and parameters defined at the start of section 3 of this paper, and using the formulas given in equations (28) and (29). On the other hand, the purity was obtained by using a simple model using as inputs (i) the spectral representation of the chirped XUV laser pulse (equations (30) and (31)) and the vibrational population distribution of the cationic states as extracted from the TDSE results. The agreement between the two methods shows that the transition from a pure to a mixed state as a function of the chirp parameter can be understood in a straightforward manner as a consequence of the ion + photoelectron entanglement that the use of a chirped ionization pulse induces.

$\alpha > 25$. Beyond this value of the chirp parameter, the purity is merely given by the vibrational population distribution (i.e. by the value of $\rho_{v,v}(t)$).

The dependence of the purity on the chirp parameter that is seen in figure 3 can be reproduced using a simple semi-analytical model, which is based on considering the spectral representation of the chirped XUV field, which is given by

$$\tilde{E}(\omega) = E_0 \frac{\sqrt{\pi}\tau_G}{\sqrt{1+\alpha^2}} \exp\left(i\Phi - \frac{(\omega-\omega_{\mathrm{XUV}})^2\tau_G^2}{4\left(1+\alpha^2\right)}\right) \quad (30)$$

with Φ given by

$$\Phi = -\frac{1}{2}\,\mathrm{atan}(\alpha) + \frac{\alpha\tau_G^2}{4\left(1+\alpha^2\right)}. \quad (31)$$

All other parameters in this expression have the same meaning as in equation (15).

Following the logic described in the supplementary information (https://stacks.iop.org/JPB/55/134001/mmedia) of [19], the ion + photoelectron state that is formed consists of combinations of ionic vibrational states v and photoelectrons with kinetic energy ε, and can be written as

$$\Psi_{\mathrm{ion+photoelectron}} \sim \times \sum_v \int d\varepsilon\ \psi_{\mathrm{ion},v}\psi_{\mathrm{photoelectron},\varepsilon}\tilde{E}(\varepsilon+E_v). \quad (32)$$

Using this expression for the total ion + photoelectron wave function, an expression for the reduced ionic density matrix can be given as

$$\rho_{vv'} = \int d\varepsilon\, \psi_{v\varepsilon}{\psi_{v'\varepsilon}}^* \sim \times \int d\varepsilon\, \tilde{E}(\varepsilon+E_v)\tilde{E}^*(\varepsilon+E_{v'})\sqrt{P_vP_{v'}}. \quad (33)$$

In this expression P_v and $P_{v'}$ represent the populations of the cationic vibrational states produced by the XUV photoionization process, which are independent of the value of the chirp parameter, and which were extracted from the TDSE calculation for $\alpha = 0$.

The purity of the ion + photoelectron wavefunction derived from the expression for the reduced ionic density matrix shown in equation (33) is plotted as a red line in figure 3, and shows that the dependence of the purity on the chirp parameter is connected in a straightforward manner to the dependence of the spectral amplitude of the XUV laser pulse on the chirp parameter, as described by equations (30) and (31).

4. Conclusions and outlook

In this paper, and in our previous theoretical and experimental papers on control of ion + photoelectron entanglement using a sequence of two attosecond laser pulses [17, 19], we have analyzed the role of ion + photoelectron entanglement as a factor limiting the degree of vibrational coherence in XUV + UV or XUV + IR pump-probe experiments targeting observation of the vibrational wavepacket dynamics in the ground state of H_2^+, following the ionization of ground state H_2 by a chirped attosecond laser pulse, respectively a sequence of two attosecond laser pulses with a variable delay. In both cases, a well-defined ion + photoelectron wavefunction is formed, which can be calculated by solving the TDSE, or about which extensive information can be obtained using a fragment ion + photoelectron coincidence measurement. Such an elaborate experimental protocol significantly goes beyond the experimental protocols that are typically used in attosecond pump-probe experiments, where experiments are commonly limited to measurements of either the photoelectrons or (fragment) ions that are formed in the experiment. The present work and the work previously published in [17, 19] shows that the coherence that underlies such a restricted experimental protocol can be severely limited by entanglement between the ion and its accompanying photoelectron. This entanglement may prevent the observation of coherent dynamics in the ion, whenever the properties of the ionic wave packet depend on the properties of the accompanying photoelectron. This situation arose in [17, 19], where a vibrational wave packet was formed in the $1s\sigma_g$ electronic state of H_2^+ by ionizing H_2 with an XUV two-pulse sequence, and where for selected XUV-XUV delays the ionization led to the formation a mixed state, where some photoelectron energies correlated with the formation of a vibrational wave packet containing only even vibrational states,

whereas other photoelectron energies correlated with the formation of a vibrational wave packet containing only odd vibrational states. Like in the current work, the vibrational wave packet was probed in [17, 19] via dissociation at the outer turning point using a short UV or NIR probe laser pulse, and the dynamics of both of the odd-v and even-v vibrational wave packets could be recovered by a determination of the pump-probe delay dependent H^+ fragment kinetic energy distribution in coincidence with the energy or momentum of the accompanying photoelectron. In the present work, we have considered the role of a chirp of the attosecond XUV pulse, and have observed that it can induce a similar transition from a pure to a mixed state, with the vibrational dynamics becoming hidden from observation, unless one again resorts to a coincident measurement of the photoelectron kinetic energy or momentum.

The behavior that we have described in [17, 19] and in the present paper is by no means specific to H_2, and is expected to be common in attosecond experiments, especially whenever the pump-probe measurements do not lead to a full characterization of the wave function of the system, but rather, address only a part of the total quantum system, such as the (fragment) ions *or* the photoelectrons, but not both at the same time. In this case, unobserved degrees of freedom may be entangled with the observed ones, and are averaged over in the experiment. In case of entanglement, which will happen whenever the total wave function cannot be written as a single direct product of wave functions for the observed and unobserved parts, this averaging amounts to taking the trace (in the density matrix) over the unobserved degrees of freedom, and this operation may remove the ability to observe the coherent dynamics of interest. Therefore, we conclude that the design of attosecond experiments requires careful consideration of the possible role that ion + photoelectron entanglement can play, and the use of measurements protocols that circumvent this role.

Data availability statement

The data that support the findings of this study are available upon reasonable request from the author.

ORCID iDs

Marc J J Vrakking https://orcid.org/0000-0002-3249-1663

References

[1] Einstein A, Podolsky B and Rosen N 1935 Can quantum-mechanical description of physical reality Be considered complete? *Phys. Rev.* **47** 777–80

[2] Bell J S 1964 On the Einstein podolsky Rosen paradox *Physics* **1** 195–200

[3] Freedman S J and Clauser J F 1972 Experimental test of local hidden-variable theories *Phys. Rev. Lett.* **28** 938–41

[4] Aspect A, Dalibard J and Roger G 1982 Experimental test of Bell's inequalities using time-varying analyzers *Phys. Rev. Lett.* **49** 1804–7

[5] Nielsen M A and Chuang I L 2010 *Quantum Computation and Quantum Information: 10th Anniversary Edition* (Cambridge: Cambridge University Press)

[6] Ekert A K 1991 Quantum cryptography based on Bell's theorem *Phys. Rev. Lett.* **67** 661–3

[7] Shor P W 1994 Algorithms for quantum computation: discrete logarithms and factoring *Proc. 35th Annual Symp. Foundations of Computer Science*

[8] Bouwmeester D, Pan J-W, Mattle K, Eibl M, Weinfurter H and Zeilinger A 1997 Experimental quantum teleportation *Nature* **390** 575–9

[9] Schlosshauer M 2007 *Decoherence and the Quantum-to-Classical transition* (*The Frontiers Collection*) ed A C Elitzur *et al* (Berlin: Springer)

[10] Zurek W H 1981 Pointer basis of quantum apparatus: into what mixture does the wave packet collapse? *Phys. Rev.* D **24** 1516–25

[11] Zurek W H 1991 Decoherence and the transition from quantum to classical *Phys. Today* **44** 36–44

[12] Akoury D *et al* 2007 The simplest double slit: interference and entanglement in double photoionization of H_2 *Science* **318** 949–52

[13] Pabst S *et al* 2011 Decoherence in attosecond photoionization *Phys. Rev. Lett.* **106** 053003

[14] Ruberti M 2019 Onset of ionic coherence and ultrafast charge dynamics in attosecond molecular ionisation *Phys. Chem. Chem. Phys.* **21** 17584–604

[15] Nishi T, Lötstedt E and Yamanouchi K 2019 Entanglement and coherence in photoionization of H_2 by an ultrashort XUV laser pulse *Phys. Rev.* A **100** 013421

[16] Karamatskou A *et al* 2020 Suppression of hole decoherence in ultrafast photoionization *Phys. Rev.* A **101** 043405

[17] Vrakking M J J 2021 Control of attosecond entanglement and coherence *Phys. Rev. Lett.* **126** 113203

[18] Agostini P and DiMauro L F 2004 The physics of attosecond light pulses *Rep. Prog. Phys.* **67** 813–55

[19] Koll L-M *et al* 2022 Experimental control of quantum-mechanical entanglement in an attosecond pump-probe experiment *Phys. Rev. Lett.* **128** 043201

[20] Scrinzi A 2012 t-SURFF: fully differential two-electron photoemission spectra *New J. Phys.* **14** 085008

[21] Yue L and Madsen L B 2013 Dissociation and dissociative ionization of H_2^+ using the time-dependent surface flux method *Phys. Rev.* A **88** 063420

[22] Olivares-Pilón H and Turbiner A V 2018 H_2^+, HeH and H_2: approximating potential curves, calculating rovibrational states *Ann. Phys., NY* **393** 335–57

[23] Bunkin F V and Tugov I I 1973 Multiphoton processes in homopolar diatomic molecules *Phys. Rev.* A **8** 601–12

[24] Stimson S *et al* 2007 Rotationally resolved vacuum ultraviolet pulsed field ionization-photoelectron vibrational bands for $HD^+(X^2\Sigma_g^+, v^+ = 0–20)$ *J. Chem. Phys.* **126** 164303

[25] Kelkensberg F *et al* 2009 Molecular dissociative ionization and wave-packet dynamics studied using two-color XUV and IR pump-probe spectroscopy *Phys. Rev. Lett.* **103** 123005